Applied Surface Science 455 (2018) 821–830

Contents lists available at ScienceDirect

Applied Surface Science

journal homepage: www.elsevier.com/locate/apsusc

Full Length Article

Evaluating oxidation behavior of amorphous aluminum phosphate coating

F.S. Sayyedan*, M.H. Enayati

Department of Materials Engineering, Isfahan University of Technology, Isfahan 8415683111, Iran

ARTICLE INFO

Keywords:
Aluminum phosphate
Oxidation resistance
Amorphous
Nanocrystalline
Coating

ABSTRACT

The aim of this study was to investigate the oxidation properties of amorphous aluminum phosphate coating. Aluminum phosphate precursor solution was prepared by a sol–gel process and then applied on AISI 304 stainless steel using dip coating technique. To evaluate the oxidation behavior, samples were placed in an electrical furnace upto 1100 °C for 100 h in air with weight measurements performed at regular ten-hour intervals. Phase composition analysis of the coatings before and after cyclic oxidation process were performed by X-ray diffractometer (XRD). The surface and cross-sectional morphology of the coatings were observed using scanning electron microscopy (SEM) analysis equipped with energy dispersive spectroscopy of characteristic X-rays (EDS). The amorphous-nanocrystalline structure and distribution of nanocrystals in the amorphous matrix were studied by transition electron microscopy (TEM). According to SEM images a uniform, continuous and crack-free coating was achieved. XRD analysis as well as TEM observations showed that the amorphous structure of coating remained unchanged after annealing at 500 °C for 15 min however; an amorphous-nanocrystalline structure was obtained after annealing at 1100 °C for 1 h. Weight change measurements after 100 h oxidation test revealed that the trace of weight gain against oxidation time for both coated and un-coated substrates were parabola in nature and the range of the weight change of the bare substrate was about 30 times greater than that of observed for the aluminum phosphate coating. In general, the results showed that the synthesized amorphous aluminum phosphate is capable of surface protecting of metals/alloys against degradation at harsh environments.

1. Introduction

The most significant concerns of degradation of engineering components are surface factors including oxidation, corrosion and wear which may restrict their longevity and use. Therefore, it is essential to protect engineering parts against harsh environments using appropriate protective coatings [1].

One of the compositions with favorable properties which can be considered as a coating is aluminum phosphate ($AlPO_4$). Aluminum phosphate has low density (2.56 g/cm^3 for berlinite), high melting temperature (1800 °C) and high hardness (6.5 Mohs). It is also stable at high temperatures; as well being chemically compatible with many metals and most widely used ceramic materials including silicon carbide, alumina, and silica over a moderate range of temperatures. However, it is unsuitable to be used as a high temperature ceramic material due to the large volume changes and subsequent stresses caused by the polymorphic transformations (berlinite, tridymite, and cristobalite) [2].

Many efforts have been done in order to synthesize aluminum phosphate with amorphous structure to improve oxidation resistance and thermal stability over the past few years. Most of them considered amorphous to crystalline transition below 1000 °C. For instance, Wang et al [2] synthesized amorphous aluminum phosphate coating using ethanol, aluminum nitrate nonahydrate ($Al(NO_3)_3{\cdot}9H_2O$) and phosphorus pentoxide (P_2O_5). The coating synthesized by Wang et al started to crystallize at 900 °C. Li et al [3] synthesized amorphous aluminum phosphate using the same precursors which remained amorphous up to 900 °C.

An amorphous aluminum phosphate composition with low oxygen diffusivity and desirable corrosion resistance over 1000 °C has been recently developed by Sambasivan et al. which may provide oxidation protection for metal substrates when deposited as a coating [4,5].

Stainless steels have good strength and good resistance to corrosion and oxidation at elevated temperatures. Intermittent service temperature for stainless steel 304 is around 850 °C. Among various applications, stainless steels are nowadays widely used in exhaust pipes to improve the service life of their components, especially the upstream part of the exhaust line (manifold, down-pipe, converter shell), where temperature can reach 1100 °C [6,7].

The aim of the present study was to develop a non-stoichiometric,

* Corresponding author.
E-mail address: fs.sayyedan@ma.iut.ac.ir (F.S. Sayyedan).

https://doi.org/10.1016/j.apsusc.2018.06.087
Received 16 April 2018; Received in revised form 2 June 2018; Accepted 10 June 2018

Table 1
Chemical composition of substrate in terms of weight percent of the elements.

Element	Fe	C	Si	S	P	Mn	Ni	Cr	Mo	Cu	Nb	Ti	V
wt%	70.52	0.0455	0.295	< 0.030	< 0.007	1.52	11.3	16	< 0.050	0.164	0.0705	0.0145	0.0537

amorphous aluminum phosphate coating by the simple and low-cost sol-gel process to increase the working temperature or extend the longevity of stainless steel 304 as an inexpensive substrate. Amorphous structures can provide oxidation and corrosion resistance. By controlling the stoichiometry, metastable structures with high thermal stability can be produced that delays crystallization up to high temperatures or long times. It is expected that this coating can provide adequate protection to metal, alloy and ceramic surfaces against degradation at high temperatures over 1000 °C.

2. Materials and methods

2.1. Substrate preparation

A 1 mm thick AISI 304 stainless steel sheet was cut into samples of 20 × 20 mm^2 using a spark wire machine. The chemical composition of substrates is given in Table 1. The samples were grounded to 4000 grit SiC paper followed by polishing using 0.3 µm alumina slurry. The samples then degreased ultrasonically in acetone, ethanol and distilled water for 10 min. The substrates were chemically etched in a concentrated acid solution of HCl (37%) and H_3PO_4 (85%) mixed in equal volume fractions for 5 min in order to create micro roughness and improve wettability of the surface. All raw chemical was purchased from Sigma-Aldrich.

2.2. Coating preparation

Non-stoichiometric amorphous aluminum phosphate precursor solution was synthesized by sol-gel process. Aluminum nitrate nonahydrate ($Al(NO_3)_3{\cdot}9H_2O$, Merck, 98.5% purity), phosphorus pentoxide (P_2O_5, Merck, 98% purity) and ethanol (C_2H_5OH, Merck, 99.8% purity) were the starting materials. To synthesize the precursor solution, a certain amount of $Al(NO_3)_3{\cdot}9H_2O$ and P_2O_5 were dissolved in ethanol. The two solutions were mixed together and allowed to stir for several minutes. Polyvinylpyrrolidone (PVP, Sigma-Aldrich, molecular weight = 10,000) was added to the above solution (a 0.5 M PVP concentration) with stirring until complete dissolution. The resulting solution was then applied on the stainless steel substrates by dip coating process with a constant withdrawal rate of 15 mm·min^{-1}. The coated samples were dried in an oven at 65 °C and then annealed in air at 500 °C for 15 min. In addition to the coated samples, a separate batch of the prepared gel was dried at 65 °C for 2 h for complete dehydration, which resulted in a light yellow, fluffy gel. Finally, samples of the dried gel were subjected to annealing in air at 500 °C for 15 min or 1100 °C for 1 h, and collected at the end of the treatment for subsequent characterization.

2.3. Coating characterization

2.3.1. Oxidation resistance

Investigation of the oxidation behavior of the coated and un-coated samples were carried out in an electrical furnace at 1100 °C for 100 h in air with weight measurements of both the sample and the spalls performed at regular ten-hour intervals. The samples were placed in Al_2O_3 crucibles, oxidized at desired temperature in ambient air, and cooled to room temperature. The weight change of samples after each thermal cycle was measured by an electrical balance with a sensitivity of ± 0.1 mg. The weight gain per unit area (ΔW/A, mg·cm^{-2}) was calculated by Eq. (1).

$$\Delta W/A = (W_i - W_0)/A \quad (1)$$

where W_i (mg) was the weight of the sample after each cycle, W_0 (mg) was the initial weight of the sample before oxidation test, and A (cm^2) was the surface area of the specimen exposed to oxidizing atmosphere.

2.3.2. XRD analysis

Phase composition analysis of the synthesized powder, coatings and oxidized samples were performed by an X-ray diffractometer (XRD, Philips PW1830) using Ni filtered Cu Ka (lCu Ka = 0.154 nm, radiation at 40 kV and 40 mA) over the 2θ range of 10–90° (time per step: 1.25 s and step size: 0.051). The Grazing Incidence XRD (GIXRD) scan was collected with a grazing incidence angle of 0.8° for the coated samples to produce an intense signal from the film and not the substrate. XRD spectra were compared to standards compiled by the Joint Committee on Powder Diffraction and Standards (JCDPS).

2.3.3. SEM, EDS and GDOES investigations

The Surface and cross section morphologies of the coatings and the oxidized samples were observed using scanning electron microscopy (SEM, using either a Zeiss EVO 50 EP equipped with energy dispersive X-ray spectrometer (EDS) or a Stereoscan 360 Cambridge instrument). Glow discharge optical emission spectrometry (GDOES, GDA 750 HR) technique operated at 700 V and regulated pressure of 2.3 hPa was performed to assess the composition and thickness of the coating.

2.3.4. TEM studies

The amorphous-nanocrystalline structure of the synthesized powder and distribution of nanocrystals in the amorphous matrix were studied by TEM (Philips-CM200 FE) technique. The powder sample for TEM observation was prepared by dispersing the powder in methanol and adding a few drops of the suspension on carbon coated TEM grid. Complementary processing of images was carried out by ImageJ where needed.

3. Results and discussion

3.1. Synthesized powder characterization

3.1.1. Phase composition analysis

The XRD patterns of the synthesized powder after drying at 65 °C for 2 h, annealing at two different temperatures, namely, 500 °C for 15 min and 1100 °C for 1 h, are shown in Fig. 1.

It is seen that the structure of the synthesized powder evolves by heat treatment. The as-synthesized dried gel does not show any crystalline feature and is characterized by a broad hump at low 2θs (between 20° and 30°), indicative of amorphous nature. Whereas calcination at 500 °C does not remarkably modify the pattern except appearance of minor crystalline diffractions around 26°, 37° and 46°, calcination at 1100 °C however clearly promotes the crystallization of the sample as demonstrated by $AlPO_4$ and Al_2O_3 peaks, supposedly embedded in the parent amorphous aluminum phosphate matrix. The initial hump at low 2θs has not disappeared however, that along with low intensity crystalline peaks, suggest a mixed amorphous-nanocrystalline structure.

3.1.2. TEM investigations

TEM bright field images and selected area electron diffraction (SAED) patterns of aluminum phosphate gel dried at 65 °C for 2 h,

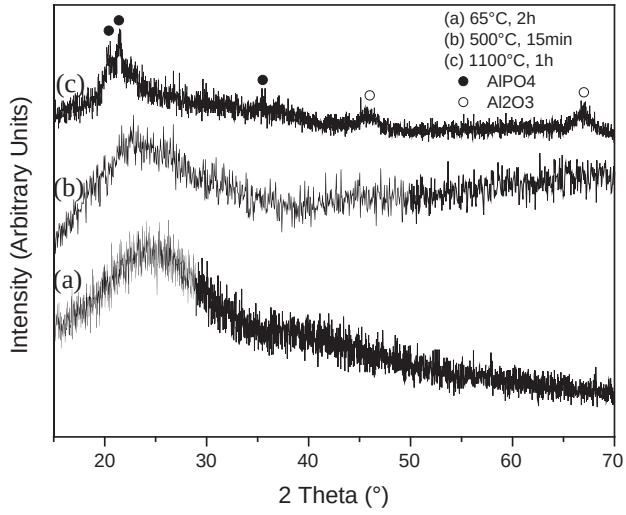

Fig. 1. XRD patterns of the synthesized aluminum phosphate (a) gel dried at 65 °C for 2 h and powder annealed at (b) 500 °C for 15 min and (c) 1100 °C for 1 h.

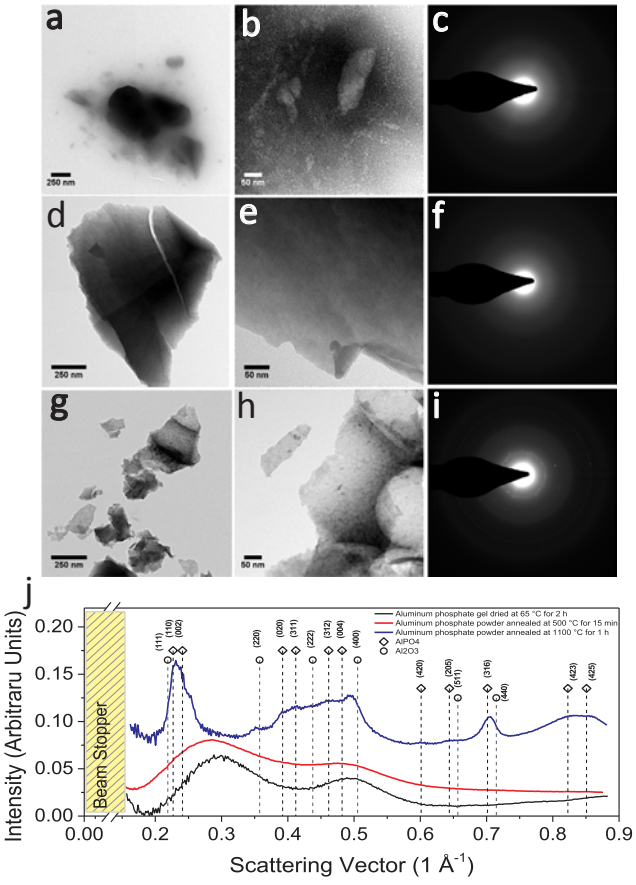

Fig. 2. (a) TEM, (b) HRTEM and (c) SAED of aluminum phosphate gel dried at 65 °C, (d) TEM, (e) HRTEM and (f) SAED of aluminum phosphate powder annealed at 500 °C for 15 min, (g) TEM, (h) HRTEM and (i) SAED of aluminum phosphate powder calcined at 1100 °C for 1 h, and (j) diffraction pattern intensity profile of the three samples.

annealed at 500 °C for 15 min and 1100 °C for 1 h are shown in Fig. 2.

The dried gel is composed of micrometer scale particles (Fig. 2a) with indistinct edges, suggesting insufficiency of drying treatment for any crystalline phase formation. High resolution TEM (HRTEM) image of this sample (Fig. 2b) confirms lack of crystallinity revealed by absence of atomic fringes, though demonstrates presence of smaller constituents, supposedly, aggregated products of sol-gel, in the big particles. SAED image of this sample (Fig. 2c) does not show crystalline rings or spots, confirming once more amorphous nature of the product in agreement with HRTEM (Fig. 2b) and XRD (Fig. 1a) results. The indistinct intensity variation in SAED of this sample forming a halo like feature, hardly corresponds to any crystalline plane of expectable materials as revealed in diffraction pattern intensity profile (Fig. 2j). The annealed sample at 500 °C, in contrast to the dried gel, shows clear and distinct particles (Fig. 2d) with almost the same size as the dried gel. Annealing has decomposed volatile residues of sol-gel process such as nitrates and organics that leads to clear observation of the powder particles. Nevertheless, HRTEM image of this sample (Fig. 2e) as well as its SAED (Fig. 2f) do not show signs of crystallinity. The diffraction pattern intensity profile of this sample (Fig. 2j) shows slight variation with respect to the dried gel, by minor shift of the broad intensity peaks to lower scattering vectors. Although this confirms the influence of annealing treatment on the atomic organization of the products, the extent of modification has been insufficient to establish any remarkable long range crystalline order. Fig. 2g and h show the products of calcination at 1100 °C, demonstrating clear changes in appearance of the powders in both micro- and nano-scale, respectively. The big particles have fragmented into smaller ones (compare Fig. 2g with Fig. 2d) probably due to stresses induced by genesis of crystalline phases. Whereas the annealed powder possessed an approximate particle size of 0.5–1 μm, after calcination this approximate particle size reduces to 200 nm. Moreover, HRTEM (Fig. 2 h) as well as the dark field HRTEM (not shown here) demonstrate the presence of tiny nanocrystals in the size range of 2–10 nm, embedded in the matrix of the larger particles. These could be either Al_2O_3 nanoparticles crystallized at high temperature due to presence of excess aluminum in the sol-gel precursors, or even, $AlPO_4$ crystallites emerged as isolated islands in the matrix of the amorphous–crystalline products. SAED image of this sample (Fig. 2i) clearly reveals crystalline rings and spots that when looked at in the diffraction pattern intensity profile (Fig. 2j), demonstrated the presence of both Al_2O_3 and $AlPO_4$.

The $AlPO_4$ pattern matches well with orthorhombic structure suggested by ICDD reference code 00-050-0303 [8] belonging to *C*2221space group. The aluminum oxide pattern however, deviates slightly from the standard Al_2O_3 composition and matches well with $Al_{2.144}O_{3.2}$ cubic spinel (space group $Fd\bar{3}m$) suggested by ICDD reference code 01-079-1557 [9], for γ–alumina.

It is interesting to note that the slight shift of both $AlPO_4$ and alumina compared to standard positions (indicated by the symbols and droplines), in particular, the maximum intensity peaks of both, i.e., (1 1 0) planes of $AlPO_4$ (with interplanar spacing (*d*): 4.409 Å, scattering vector: 0.227 $Å^{-1}$ and 2θ: 20.123°) and (4 4 0) planes of $Al_{2.144}O_{3.2}$ (with *d*: 1.399 Å, scattering vector: 0.715 $Å^{-1}$ and 2θ: 66.815°). This, on the one hand, suggest incomplete crystallization of the products, and on the other hand, suggests that the two phases are interconnected in the atomic scale, arguably, strongly attached and integrated in the interface of the two phases, so that a gradient is happening in the crystalline order moving from one domain to the other, and thus, a clear crystalline boundary could not be easily realized. This make more sense when considering the fact that such phenomenon is more pronounced for the crystalline planes of each phase that share a *d* similar to one of those of the other phase. For instance, (1 1 0) planes of $AlPO_4$ have a *d* similar to (1 1 1) planes of $Al_{2.144}O_{3.2}$, and (4 4 0) planes of $Al_{2.144}O_{3.2}$ have a *d* similar to (3 1 6) planes of $AlPO_4$. Crystalline integrity of these two phases along the above mentioned crystalline planes is an interesting subject for further investigations.

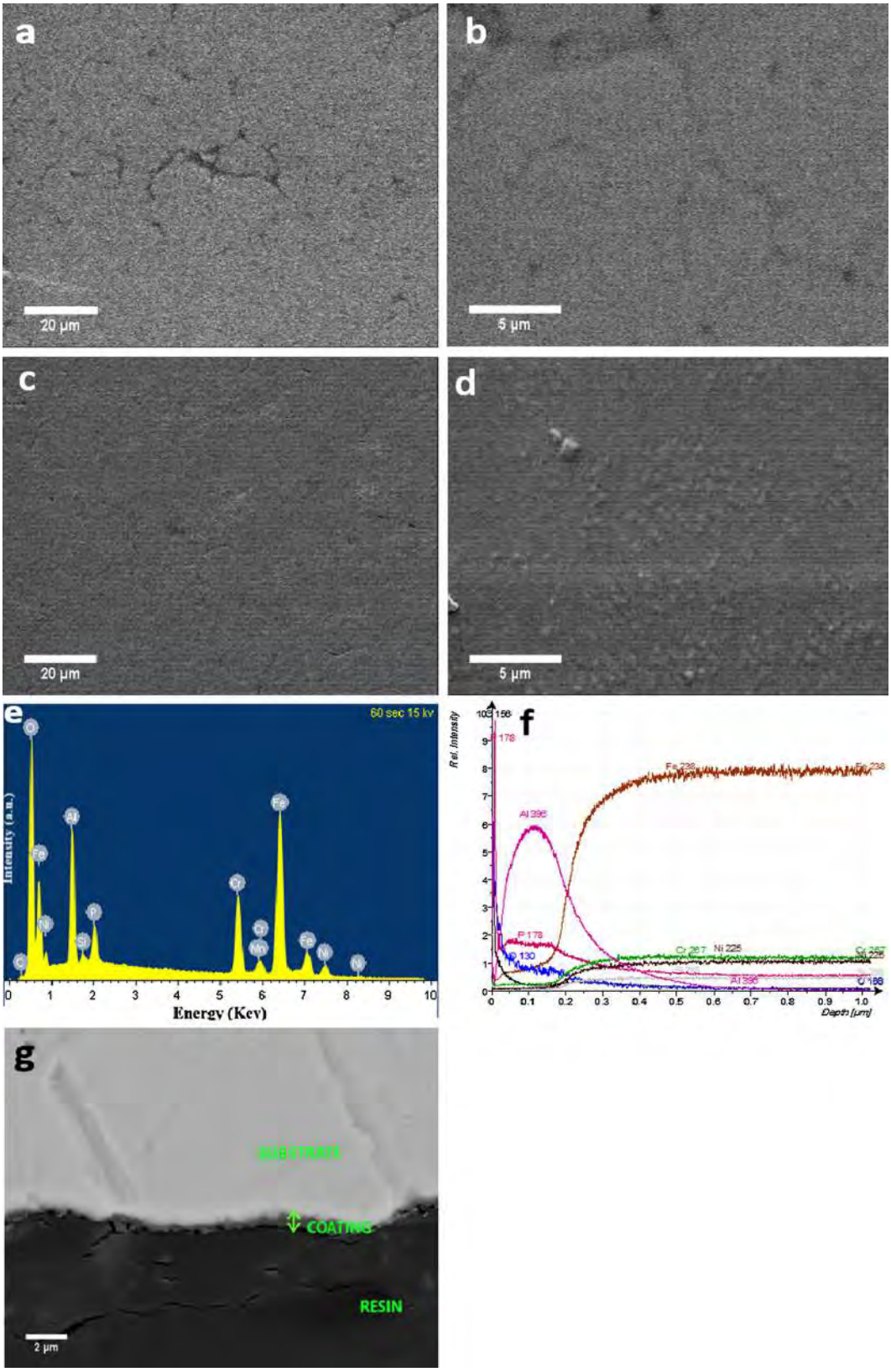

Fig. 3. Surface image, EDS and GDOES analyses of the amorphous aluminum phosphate coating formed on stainless steel 304 after drying and annealing steps: (a) and (b) surface morphology after drying at 65 °C for 2 h at two different magnifications, (c) and (d) surface morphology after annealing at 500 °C for 15 min at two different magnifications, (e) EDS analysis after annealing at 500 °C for 15 min, (f) GDOES analysis after annealing at 500 °C for 15 min, (g) cross section morphology of coating after annealing at 500 °C for 15 min.

3.2. Coating characterization

3.2.1. Microstructure and elemental composition analysis

Fig. 3 exhibits the SEM micrographs, EDS and GDOES analyses of the amorphous aluminum phosphate coating formed on stainless steel 304 after drying at 65 °C for 2 h and annealing at 500 °C for 15 min.

Etching effect of the grain boundaries is immediately evident from Fig. 3a and b. As seen in SEM micrographs of dried (Fig. 3a and b) and annealed (Fig. 3c and d) samples, the coating is uniform and continuous. Moreover, except in the vicinity of the edges where adhesion and accumulation of the solution onto the sample surface is not necessarily regular, very scarce symptoms of cracking could be observed in the central regions. It should be noted that sample preparation procedure and sol-gel composition adjustment were carefully controlled to achieve such level of coating integrity. These include, controlled roughness of the specimens, fine-tuned content of the PVP additive, and finally, the heating and cooling rates during annealing.

EDS analysis of the annealed coating (Fig. 3e) confirms the presence of aluminum phosphate layer revealed by clear Al and P peaks. Furthermore, GDOES analysis (Fig. 3f), demonstrates firstly, that Al and P elements, have a meaningful concentration gradient in the surface region, decaying towards the depth, and secondly, that the approximate thickness of the layer is around 300 nm, where the Fe, Cr and Ni contents are almost constant. Fig. 3g shows the cross-sectional microstructure of the coating after annealing at 500 °C for 15 min. It can be found that the coating is dense, uniform, with good adhesion to the substrate. The thickness of the coating is estimated to be 300 nm which is in accordance with GDOES result.

Film stability under thermal cycling conditions is critically important for many applications and the thin nature of these films will help to minimize the residual thermal stresses such that cracking and spallation is prevented [10].

3.3. Oxidation resistance

3.3.1. Phase composition analysis

Fig. 4 illustrates the XRD pattern of the pristine AISI 304 stainless steel as the substrate. The peaks at 44°, 51° and 75° in the pristine sample are related to γ-Fe (austenite) phase in AISI 304 stainless steel [11,12].

Fig. 5 presents the GIXRD patterns of the oxidized substrate and the coated one after cycle 1 (oxidation at 1100 °C for 10 h) and cycle 10 (oxidation at 1100 °C for 100 h).

The effect of 10 h oxidation at 1100 °C on uncoated sample is apparent as revealed by the majority of Fe_2O_3 peaks. Additionally,

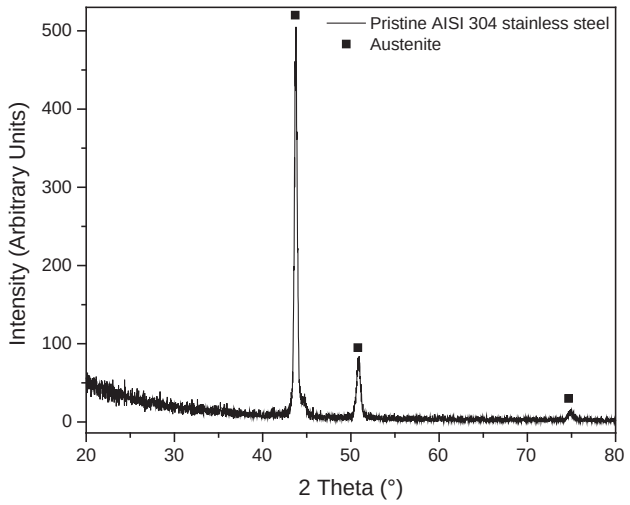

Fig. 4. XRD pattern of pristine AISI 304 stainless steel.

alloying elements of the AISI 304 stainless steel such as Cr and Mn have remarkably contributed in the formation surface oxide layer as demonstrated by Cr_2O_3, $MnCr_2O_4$ and $FeCr_2O_4$ peaks. The oxide layer is apparently thick since the reflections from the austenite substrate are not observed anymore. The protective effect of aluminum phosphate against high temperature oxidation could be realized in comparison between the coated and uncoated samples, where the oxide peaks and their intensity have remarkably decreased in the coated one. Such capability is attributed to the low oxygen diffusivity of this compound [4]. Comparing to the bare substrate, the spinel oxide peaks, namely, $MnCr_2O_4$ and $FeCr_2O_4$, are dominant in coated sample, indicating the more oxidation resistance of the coated substrate than the bare one. It is notable that spinel oxides are complex compounds which prevent diffusion of cations through the oxide layer and thus, decelerate the oxidation rate [13].

In addition, no obvious diffraction peak corresponding to $AlPO_4$ could be observed in this sample. This implies the dominant amorphous nature of the coating and on the other hand, suggests possible overshadowing of the minor crystalline $AlPO_4$ contributions by the major amorphous ones as well as the abundant metal oxide phases. It should be pointed out that the oxidized stainless steel after cycle 10, is mainly consisted of Fe_2O_3, indicating the chromium depletion of the substrate-oxide interface by evaporation of chromium volatile species (CrO_3) [6]. It means that there is not sufficient chromium content to form the protective chromium oxide film on the surface, which leads to nucleation of non-protective Fe-rich oxide, and results in an increase of oxidation rate [7]. This behavior is further confirmed by weight gain plots presented in Section 3.3.3.

3.3.2. Macro- and micro-structure analyses

Surface morphology and EDS analyses of the bare substrate and the coated one after oxidation at 1100 °C for 10 h and 100 h are presented in Fig. 6.

The oxidized outer surface of the uncoated stainless steel 304 indicates irregular and non-faceted features (Fig. 6a and c), while the coated one presents regular equiaxed grains with faceted margins (Fig. 6e and g).

Apparently, such morphological features of hematite oxide particle differ from those of spinel particle having straight sides and planar faces [14].

According to Kuang et al's TEM and SEAD patterns observations [14] the faceted oxide particles in the oxide scale grown on the stainless steel 304 have a spinel structure that have been detected as $FeCr_2O_4$ and $MnCr_2O_4$ in the XRD patterns of the coated surface (Fig. 5a and c). In contrast, shapeless and non-faceted oxide particles show a hematite structure, which are mainly composed of Fe_2O_3 according to XRD patterns of un-coated surface (Fig. 5b and d). Surface analysis by XRD revealed that the main oxide products on the coated surface were $FeCr_2O_4$ together with some Fe_2O_3, while for the bare substrate, Fe_2O_3 was the main product together with a small amount of $FeCr_2O_4$. These observations seem to be promising for the coated samples in this research, as spinel oxides could be considered as protective oxides and hematite oxides as non-protective ones [13].

Moreover, it can be seen that the outer surface of the oxide layer of the aluminum phosphate coated substrate, has a similar aspect after 10 h and 100 h exposure at 1100 °C. The growth of the oxide crystallites is somewhat observed after 100 h exposure (from ~1 μm to ~2 μm) (Fig. 6e and g). Concerning the bare substrate, the significant difference is observed between 10 h and 100 h exposure (Fig. 6a and c). In agreement with the XRD results, Fe_2O_3 is mainly present on the outer surface of the 304 stainless steel when oxidized at 1100 °C for 100 h (Fig. 5d). The protrusions of Fe_2O_3 are apparent in Fig. 6c which is attributed to the higher mobility of Fe than Cr [15]. Fe_2O_3 bulges grow and pass through the already formed chromia film on the surface. The oxidation mechanism of the coated and un-coated samples is described in Section 3.3.3.

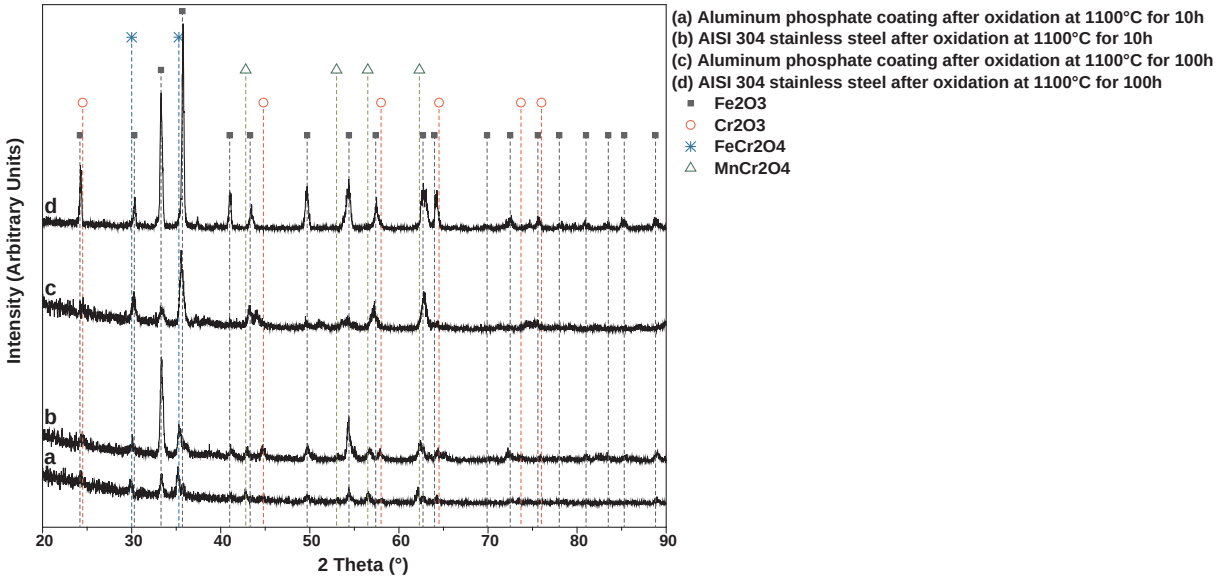

Fig. 5. GIXRD patterns of (a) Aluminum phosphate coating after oxidation at 1100 °C for 10 h, (b) AISI 304 stainless steel after oxidation at 1100 °C for 10 h, (c) aluminum phosphate coating after oxidation at 1100 °C for 100 h, and (d) AISI 304 stainless steel after oxidation at 1100 °C for 100 h.

The EDS results are in agreement with the XRD patterns and suggest that the metal elements (Fe, Cr and Mn) on the stainless steel surface have been oxidized. Combined with XRD results, the formed oxide crystallites are mainly consisted of Fe_2O_3 and $FeCr_2O_4$ and a small amount of Cr_2O_3 and $MnCr_2O_4$. EDS results of un-coated surface after 10 h and 100 h exposure at 1100 °C (Fig. 6b and d) reveals a reduction in chromium content and an increase in iron content with increasing the exposure time, implying the volatilization of chromium species followed by chromium depletion in the substrate-oxide interface and expedition in growth of iron oxide [6].

In contrast, comparing the EDS results of coated surface after 10 h and 100 h exposure at 1100 °C (Fig. 6f and h) shows almost no obvious difference in Cr and Fe contents, signifying that the surface is still enriched in chromium even after 100 h exposure at 1100 °C and a protective chromia film could be formed.

Fig. 7 shows the digital photographs of the bare and aluminum phosphate coated substrate after oxidation at 1100 °C for 100 h. The coated substrate exhibited no obvious spallation in coating through the entire oxidation test, while the uncoated substrate underwent a great deal of weight gain followed by the spallation of top oxide layers in multiple times. Oxidized after 10 cycles, remarkable breakage and massive peeling-off were observed on the surface of the bare substrate.

Fig. 8 demonstrates the cross-sectional microstructure of the bare stainless steel 304 after oxidation at 1100 °C for 10 h and the aluminum phosphate coated substrate after oxidation at 1100 °C for 10 h and 100 h. It should be noted that after 100 h thermal cyclic oxidation, the

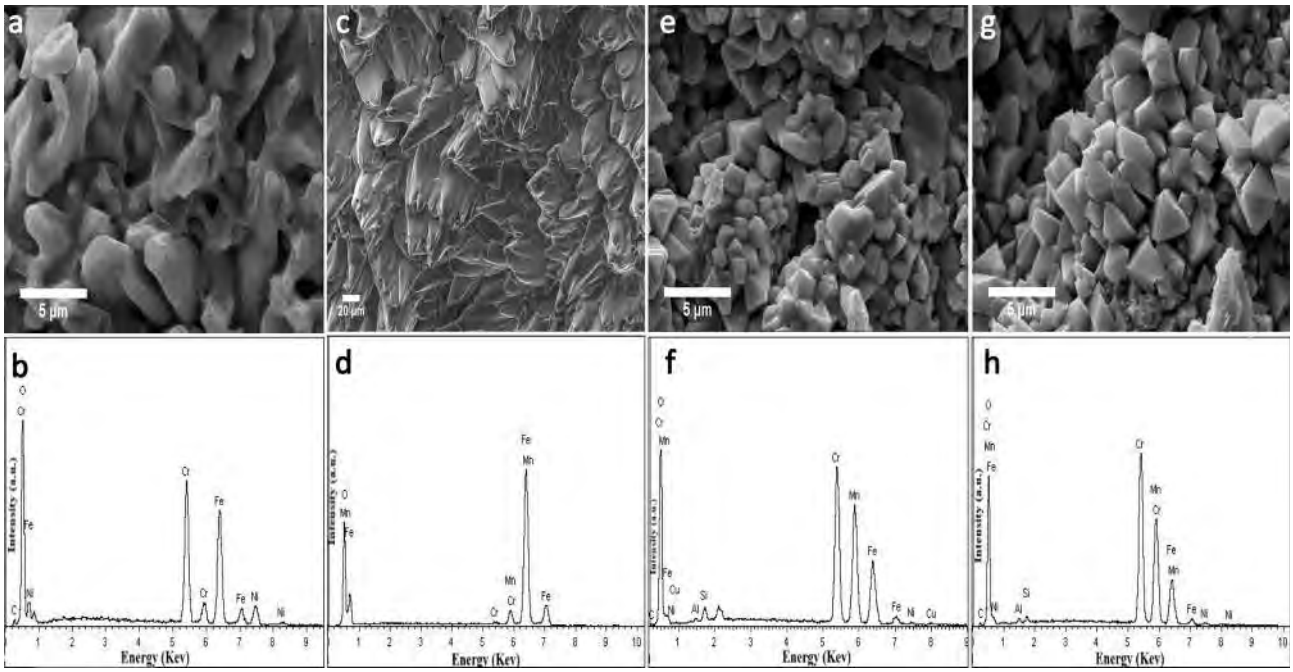

Fig. 6. (a) SEM image of AISI 304 stainless steel after oxidation at 1100 °C for 10 h, (b) EDS analysis of (a), (c) SEM image of AISI 304 stainless steel after oxidation at 1100 °C for 100 h, (d) EDS analysis of (c), (e) SEM image of aluminum phosphate coating after oxidation at 1100 °C for 10 h, (f) EDS analysis of (e), (g) SEM image of aluminum phosphate coating after oxidation at 1100 °C for 100 h, (h) EDS analysis of (g).

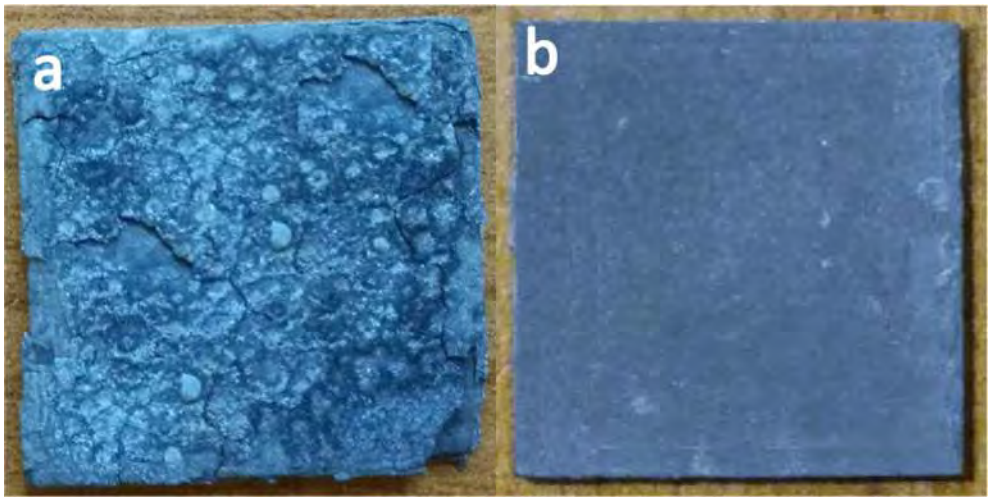

Fig. 7. Digital photographs after oxidation at 1100 °C for 100 h: (a) Bare stainless steel 304, (b) aluminum phosphate coated stain less steel 304.

bare substrate completely failed due to alternate formation and spallation of the oxide scales, somehow that the cross-sectional study was not possible.

The convoluted interface in Fig. 8 for both coated and un-coated surfaces reveals that the process controlling the oxidation parabolic rate is diffusion through the oxide scale [16]. The thickness of the oxide layer formed on the surface of the bare substrate after 10 h oxidation is estimated 30 μm, while it is around 6 μm and 11 μm for the coated surface after 10 h and 100 h the cyclic oxidation, respectively. According to Fig. 8b and 8c, the integrity of the oxide layer formed on the surface is maintained after 10 h and even 100 h cyclic oxidation, whereas the oxide scale formed on the bare stainless steel after 10 h tends to be detached from the surface, as the crack propagation path in the thickened oxide scale is shown by white arrows in Fig. 8a. In contrast, from the cross-sectional images of coated surface (Fig. 8b and 8c), it can be seen that the oxide layer remained well adhered to the alloy substrate.

3.3.3. Weight change measurements

Fig. 9 represents the measured weight changes per unit area of the bare stainless steel 304 and aluminum phosphate coated substrate plotted against the oxidation time. The weight change of the coated substrate against the oxidation time is separately plotted in inset of Fig. 9a for clearer demonstration of oxidation behavior of the coating material. Quadratic plots of the weight variation against the oxidation time for both coated and un-coated surfaces are also plotted in Fig. 9b and c to establish the rate law for oxidation.

It is immediately evident from Fig. 9a that the weight gain of the coated sample (4 mg·cm^{-2}) is remarkably lower than the bare one (120 mg·cm^{-2}), signifying the protective effect of the applied aluminum phosphate coating due to retarding the inward-diffusion of oxygen and outward-diffusion of iron [17]. It is also observed that both coated and un-coated surfaces follow a similar trend of weight gain during cyclic oxidation process, although the coating has a major kinetic effect and retards the scale spallation, as the obtained weight gain of the bare substrate was almost 30 times greater than that of the coated samples.

Referring again to Fig. 9a shows that a parabolic law given by Eq. (2), was obeyed for the oxidation of coated and un-coated stainless steel 304, indicating that the diffusion process through the oxide layer prevailed during oxidation [6,18].

$$(\Delta W/A)^2 = a + k_p t \quad (2)$$

where ΔW (mg) is the weight gain, A (cm^2) is the surface area of the specimen exposed to oxidizing atmosphere, K_p (mg^2·cm^{-4}·h^{-1}) is the parabolic rate constant, t (h) is the oxidation time and a is a constant.

When plotting the kinetic curves at 1100 °C in quadratic coordinates, two successive stages appear, as shown in Fig. 9b and c, each of them follows a parabolic law. The change of the slope was found after 50 h and 60 h exposure at 1100 °C for the bare substrate and the coated one, respectively. Fig. 10 represents the K_p values of the coated and uncoated substrates during different time intervals of cyclic oxidation process. It is clear that the K_p values for the coated substrate are significantly lower than that of the bare one, corresponding to the

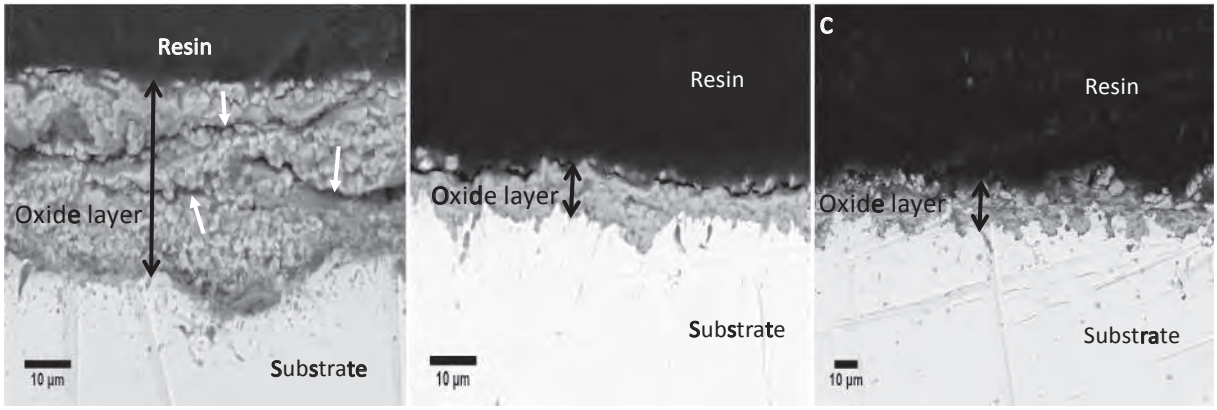

Fig. 8. Cross-sectional microstructure of (a) AISI 304 stainless steel after oxidation at 1100 °C for 10 h, (b) aluminum phosphate coating after oxidation at 1100 °C for 10 h, (C) aluminum phosphate coating after oxidation at 1100 °C for 100 h.

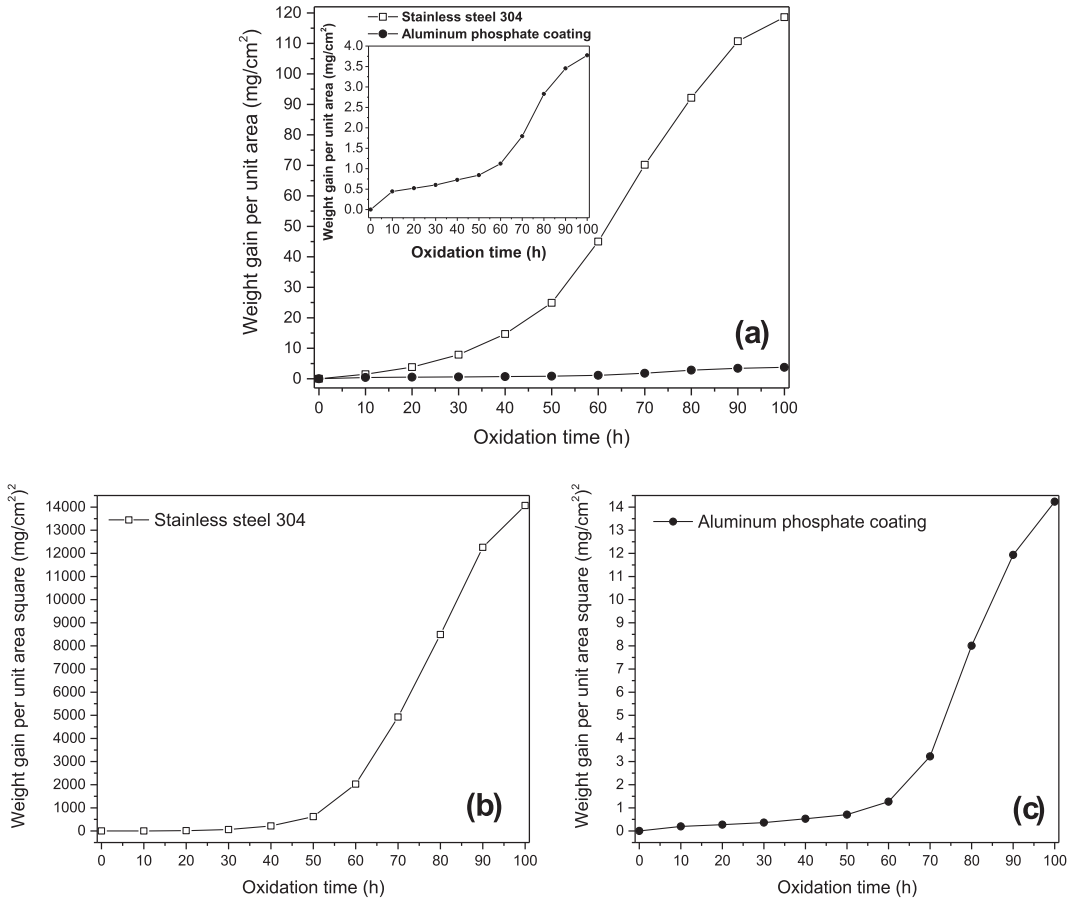

Fig. 9. (a) Weight gain per unit area vs. oxidation time for AISI 304 stainless steel and aluminum phosphate coating (inset: weight change per unit area of aluminum phosphate coating vs. oxidation time), Square of weight gain per unit area vs. oxidation time for: (b) AISI 304 stainless steel (c) aluminum phosphate coating.

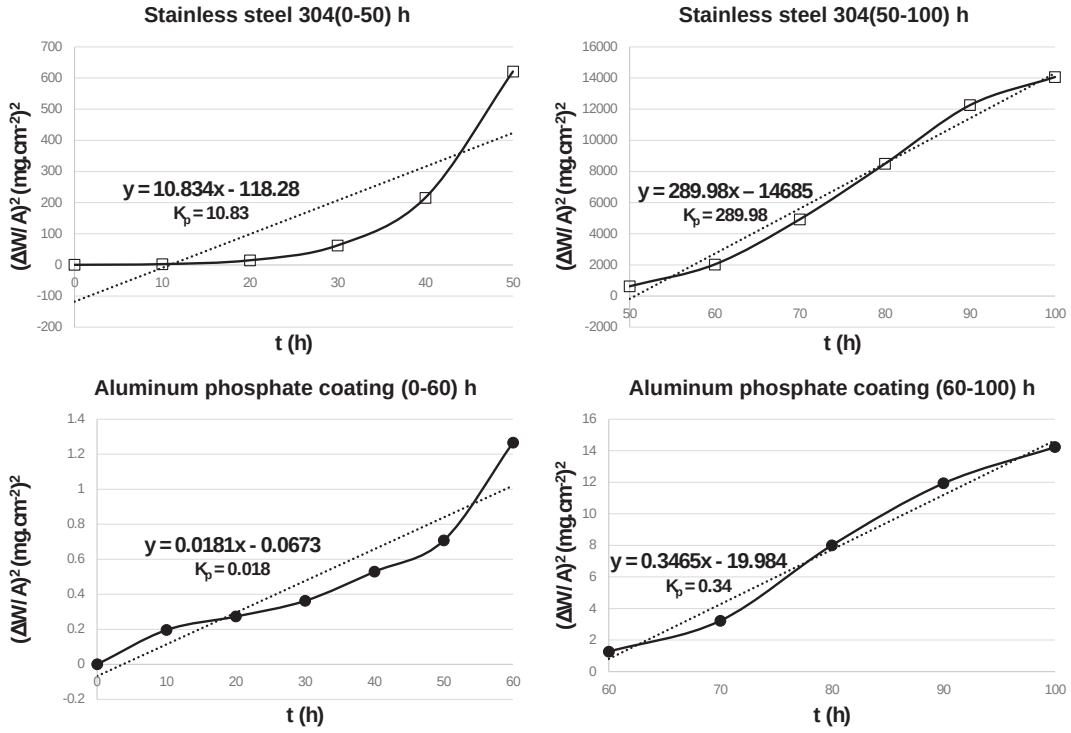

Fig. 10. The trend lines of the kinetic curves during different time intervals of cyclic oxidation process at 1100 °C for coated and un-coated substrates.

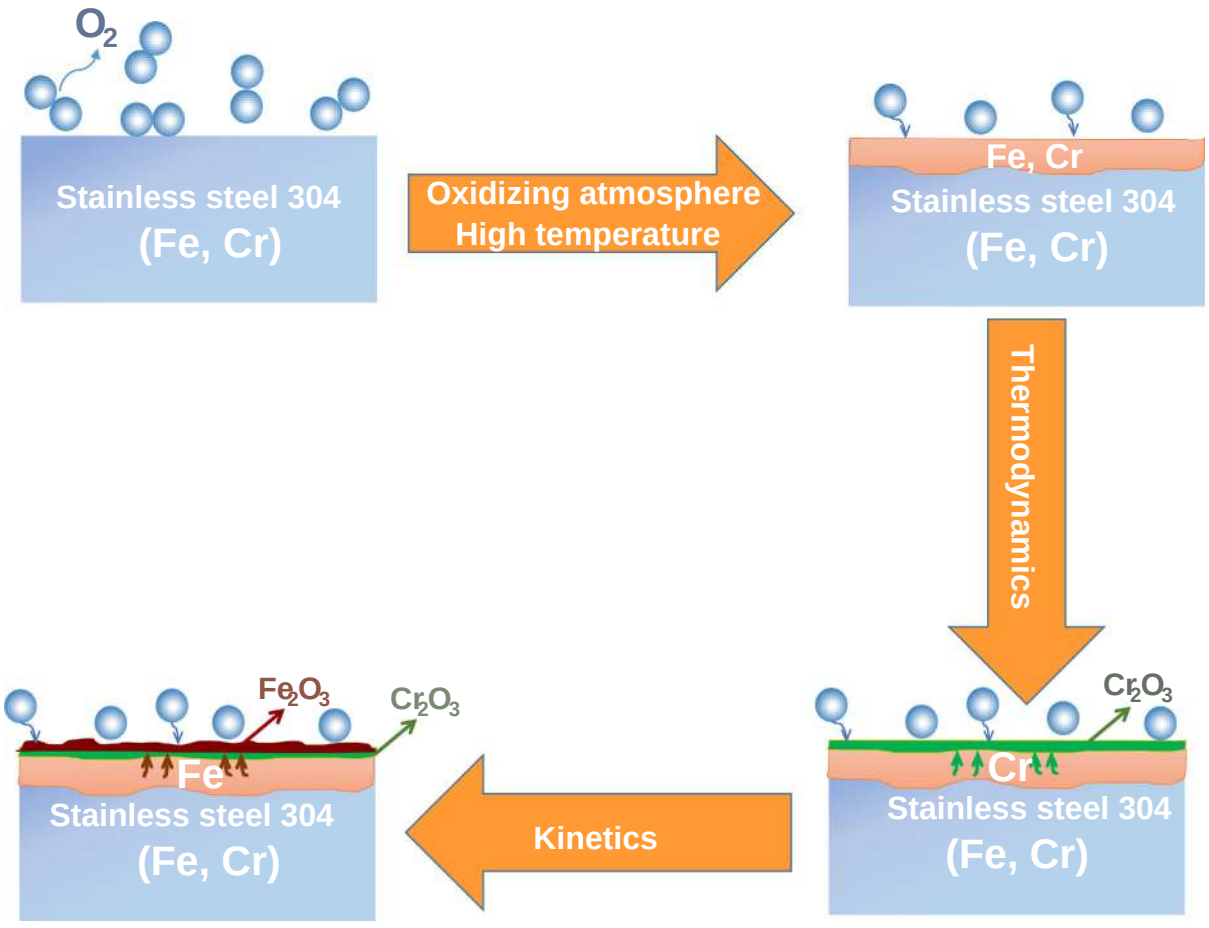

Fig. 11. Schematic diagram of oxidation process and mechanism of the stainless steel 304 in air.

superior oxidation resistance of the coated sample.

Based on the results' series presented, the oxidation mechanism of stainless steel 304 is schematically shown in Fig. 11 and can be summarized as follows.

According to the classical thermodynamic theory, if the standard Gibbs free energy change (ΔG°) is less than zero, the products are thermodynamically stable, and the reaction proceeds spontaneously. The relations between the standard Gibbs free energy change for two main oxides formed on the stainless steel (Fe_2O_3 and Cr_2O_3) at temperature T is given by Eqs. (3) and (4) [15].

$$\Delta G^{\circ}(Fe_2O_3) = -543.349(J{\cdot}mol^{-1}) + 167.4(J{\cdot}mol^{-1}{\cdot}K^{-1})T \quad (3)$$

$$\Delta G^{\circ}(Cr_2O_3) = -746.844(J{\cdot}mol^{-1}) + 173.2(J{\cdot}mol^{-1}{\cdot}K^{-1})T \quad (4)$$

From Eqs. (3) and (4), it is clear that ΔG° for Fe_2O_3 and Cr_2O_3 formation is zero at $T \geq 0$ and the reaction of Fe and Cr with oxygen favors in formation of Fe_2O_3 and Cr_2O_3, respectively. On the other hand, ΔG° (Cr_2O_3) is always more negative than ΔG° (Fe_2O_3), suggesting the greater affinity of oxygen to chromium. Thus, the formation of Cr_2O_3 is thermodynamically preferred, resulting in a Cr-rich surface layer at the first cycle of the oxidation (Fig. 6b) [14]. However, owing to the greater mobility of Fe ions/atoms [14,15] and the high temperature, Fe ions diffuse through the already formed Cr_2O_3 thin film to react with oxygen and form Fe_2O_3. Therefore, the formation of Fe_2O_3 is mainly controlled by the kinetics than the thermodynamics [15]. As it is seen in the last cycle of the oxidation, Fe content in the oxide film increases, while Cr content decreases (Fig. 6d), indicating the formation of Fe-rich outer layer. Fig. 6h shows that even after 100 h oxidation process, there is still a significant amount of chromium on the aluminum phosphate coated surface, indicating the possibility of formation of protective chromia film on the surface. This reveals the capability of the coating material in the formation of a barrier and protective film on the surface to decelerate diffusion of cations through the oxide layer [6].

The Cr_2O_3 layer may also evolve to a mixed iron-chromium oxide as the XRD results of the oxidized samples revealed $FeCr_2O_4$ due to Fe diffusion.

Due to the defective structure of Fe_2O_3, the outmost Fe-rich oxide particles grow up rapidly with increasing the oxidation time and finally detach from the surface due to stress concentration and the poor bond strength between thickened oxide layers [7]. This phenomenon is specified by white arrows in Fig. 8a.

The weight change of the coated substrate with oxidation time (Fig. 9a) indicates that it follows a similar mechanism with a significantly lower rate as the bare stainless steel 304 during high temperature oxidation. The kinetic control and protective effect of the applied aluminum phosphate coating in this research refer to its amorphous structure and low oxygen diffusivity due to absence of crystalline defects [19].

4. Conclusions

The amorphous aluminum phosphate coating with 300 nm thickness was prepared on stainless steel 304 alloy by means of a simple dip coating technique. After oxidation at 1100 °C for 100 h, spinel oxides were dominant on the surface of the coated sample, while hematite structure oxides quickly grew through the surface of the bare substrate, indicating the superior oxidation resistance of the coated substrate than the bare one. Also, no oxide scales were found either at coating/substrate interface or on coating surface of the coated samples, exhibiting a

significantly lower weight gain (4 $mg{\cdot}cm^{-2}$) compared with the bare substrate (120 $mg{\cdot}cm^{-2}$). The weight change of the bare and coated samples during oxidation test was found to be parabolic. A deviation to the parabolic behavior was observed, with two stages, initially formation of Cr_2O_3 followed by the growth of iron oxides which induces a greater oxidation rate. However, the value of the parabolic rate constant (K_p) in each stage was remarkably lower for the coated sample than the bare one. In general, the results showed that the applied amorphous aluminum phosphate coating could provide surface protection of metals/alloys against degradation at harsh environments.

Acknowledgments

The authors gratefully acknowledge the support of the Iran National Science Foundation (INSF) on this research under grant number 94016469. The authors also sincerely appreciate Professor Massimiliano Bestetti from Department of Chemistry, Materials and Chemical Engineering, Politecnico di Milano, Italy, for his generous supports on this research.

References

[1] K. Kokini, J. DeJongs, S. Rangaraj, B. Beardsley, Thermal shock of functionally graded thermal barrier coatings with similar thermal resistance, Surf. Coat. Technol. 154 (2002) 223–231.
[2] Y.M. Wang, H. Tian, L.X. Guo, J.H. Ouyang, Y. Zhou, D.C. Jia, Amorphous $AlPO_4$ coating formed on titanium alloy for high temperature oxidation protection: oxidation kinetics and microstructure, Surf. Coat. Technol. 252 (2014) 134–141.
[3] N. Li, M. Zhong, Zh. Xu, Zh. Zhang, Polyesterification synthesis of amorphous aluminum phosphate thermal radiation material with high infrared emissivity, Mater. Lett. 213 (2018) 335–337.
[4] S. Sambasivan, K.A. Steiner, High temperature amorphous composition based on Aluminium phosphate, U.S. Patent No. 0011245 A1, Chicago, 2004.
[5] S. Sambasivan, K. Rangan, Aluminium phosphate based microspheres, U.S. Patent No. 7,833,342 B2, Chicago, 2010.
[6] A.M. Huntz, A. Reckmann, C. Haut, C. Sévérac, M. Herbst, F.C.T. Resende, A.C.S. Sabioni, Oxidation of AISI 304 and AISI 439 stainless steels, Mater. Sci. Eng. A. 447 (2007) 266–276.
[7] D.B. Wei, J.X. Huang, A.W. Zhang, Z.Y. Jiang, A.K. Tieu, X. Shi, S.H. Jiao, X.Y. Qu, Study on the oxidation of stainless steels 304 and 304L in humid air and the friction during hot rolling, Wear 267 (2009) 1741–1745.
[8] H. Graetach, Inst. F. Mineralogie, Ruhr-Univ. Bochum, Germany, Private Communication, 1998.
[9] R.S. Zhou, R.L. Snyder, Structures and transformation mechanisms of the η, γ and θ transition aluminas, Acta Cryst. B 47 (1991) 617–630.
[10] S. Sambasivan, K.R. Steiner, K. Rangan, Aluminum phosphate coatings, U.S. Patent No. 7,311,944 B2, Chicago, 2007.
[11] Ch. Kuo, Ch. Lin, G. Lai, Y. Chen, Y. Chang, W. Wu, Characterization and mechanism of 304 stainless steel vibration welding, Mater. Trans. 48 (2007) 2319–2323.
[12] Ch. Quan, Y. He, Properties of nanocrystalline Cr coatings prepared by cathode plasma electrolytic deposition from trivalent chromium electrolyte, Surf. Coat. Technol. 269 (2015) 319–323.
[13] N. Birks, G.H. Meier, F.S. Pettit, Introduction to the High Temperature Oxidation of Metals, second ed., Cambridge University, New York, 2006.
[14] W. Kuang, E. Han, X. Wu, J. Rao, Microstructural characteristics of the oxide scale formed on 304 stainless steel in oxygenated high temperature water, Corros. Sci. 52 (2010) 3654–3660.
[15] C.Y. Cui, X.G. Cui, X.D. Ren, M.J. Qi, J.D. Hu, Y.M. Wang, Surface oxidation phenomenon and mechanism of AISI 304 stainless steel induced by Nd:YAG pulsed laser, Appl. Surf. Sci. 305 (2014) 817–824.
[16] T. Ishida, Y. Harayama, S. Yaguchi, Oxidation of 304 stainless steel in high temperature steam, J. Nucl. Mater. 140 (1986) 74–84.
[17] L. Luo, J. Yao, J. Li, J. Yu, Preparation and characterization of sol–gel Al_2O_3/Ni–P composite coatings on carbon steel, Ceram. Int. 35 (2009) 2741–2745.
[18] D. Wei, P. Zhang, Z. Yao, J. Zhou, X. Wei, P. Zhou, Cyclic oxidation behavior of plasma surface chromising coating on titanium alloy Ti–6Al–4V, Appl. Surf. Sci. 261 (2012) 800–806.
[19] J. Qi, B. Huang, Zh. Wang, H. Ding, J. Xi, W. Fu, Dependence of corrosion resistance on grain boundary characteristics in a high nitrogen Cr-Mn austenitic stainless steel, J. Mater. Sci. Technol. 33 (2017) 1621–1628.